RESEARCH ARTICLE

Gold-Oxide Nanofilms Trigger Ultrafast, Reagent-Free, Site-Confined Growth of Conducting Polyaniline

Piotr Olejnik[1] | Barbara Kupikowska-Stobba[3] | Julia Anchimowicz[1] | Marcin Strawski[4] | Barbara Palys[4] | Angelika Zaszczynska[3] | Judyta Dulnik[3] | Magdalena Stobiecka[1] | Marek Grzeskiewicz[2] | Slawomir Jakiela[1]

[1]Department of Physics and Biophysics, Warsaw University of Life Sciences, Warsaw, Poland | [2]Institute of Wood Sciences and Furniture, Warsaw University of Life Sciences, Warsaw, Poland | [3]Institute of Fundamental Technological Research, Polish Academy of Sciences, Warsaw, Poland | [4]Faculty of Chemistry, University of Warsaw, Warsaw, Poland

Correspondence: Piotr Olejnik (piotr_olejnik@sggw.edu.pl) | Slawomir Jakiela (slawomir_jakiela@sggw.edu.pl)

ABSTRACT

Conducting polymers enable the simultaneous transport of electrons and ions within soft, biocompatible matrices. Yet their synthesis typically relies on soluble oxidants that generate stoichiometric waste and inhibit high-resolution patterning. Nanometer-thick gold films deposited by direct-current magnetron sputtering in dilute air function concurrently as a template and intrinsic oxidant—though, owing to their discontinuous structure, not as current collectors—for the reagent-free growth of emeraldine-salt polyaniline (PANI-ES). X-ray photoelectron spectroscopy reveals that freshly sputtered films contain approximately 60% Au_2O_3, which is quantitatively reduced by aniline within 60 s. In situ UV–vis spectroscopy records an increase in the 750 nm polaron band that scales linearly with oxide thickness. Polymerization self-terminates once the local Au(III) reservoir is exhausted, yielding patterns precisely registered to the underlying metal mask. The resulting PANI-ES retains the optical, Raman, and electrochemical signatures of the highly conductive emeraldine salt. By replacing soluble oxidants with a solid Au_2O_3 underlayer, the process avoids sulfate-containing solution-phase by-products and enables aniline-to-PANI conversion at room temperature under ambient air, providing a straightforward route to patterned PANI films without post-growth wet lithography for hole-transport layers, neural microelectrodes, and chemiresistors.

1 | Introduction

PANI occupies a unique position among π-conjugated polymers because its redox state, protonation level, and charge transport can be post-synthetically tuned by nothing more sophisticated than the pH or electrochemical potential of the surrounding medium. Since the pioneering report by MacDiarmid, Epstein, and Heeger in 1987 [1], polyaniline and its composites have been investigated for use in anticorrosion coatings [2], electrochromic windows [3], energy storage devices [4], membranes [5], and bioelectronics [6]. Each of these applications ultimately faces the same obstacle, however: the oxidative coupling that transforms colorless aniline into the deep green, conductive emeraldine salt (ES) is usually carried out using soluble oxidants such as ammonium persulfate $(NH_4)_2S_2O_8$ [7], $AgNO_3$ [8] or $HAuCl_4$ [9]. These reagents are indiscriminate and coat every wetted surface with residues of sulfate, nitrate, or chloride salts. They also require wet lithography if spatial control is desired. While electrochemical polymerization can eliminate chemical waste, it demands a potentiostat, electrolyte containment, and pre-patterned electrodes. Vapor-phase oxidations, on the other hand, require elevated temperatures and still leave a metallic byproduct behind [10].

We therefore sought a method to combine the roles of oxidant, conductor, and hard mask in a single solid film that could be

patterned easily at room temperature. Gold offers an attractive yet under-exploited opportunity: in its zero-valent state Au is famously noble, but in its trivalent oxide (Au_2O_3) it acts as a strong oxidizing agent with a formal potential of +1.50 V vs. standard hydrogen electrode [11]. Gold(III) oxide is only moderately stable at room temperature; its formation enthalpy is endothermic ($+19.3$ kJ mol^{-1}), and its free energy of formation is near zero at 298 K, making spontaneous decomposition thermodynamically favorable [12]. Early studies showed that an Au_2O_3 layer reverts to metallic Au at 22°C with an activation barrier of ~57 kJ mol^{-1} [13], and subsequent work confirmed that Au_2O_3 on nanoparticles undergoes complete reduction below 300 K on reducible supports [12]. In other words, Au(III) in thin films is a kinetically metastable state.

Herein, we harness this behavior by using direct-current magnetron sputtering in a dilute air plasma to deposit nanometer-thick Au films that are in situ partially oxidized. The as-prepared Au/Au_2O_3 nanofilms serve as both the template and the intrinsic oxidant for reagent-free polymerization of aniline. Upon immersion in an acidic aniline solution, the Au_2O_3 is rapidly consumed to oxidize aniline into a conductive PANI-ES film, while the underlying Au nanostructure remains as a discontinuous, inert scaffold. In the following, we present a full characterization of the sputtered gold oxide films and the polyaniline layers grown thereon, and discuss the mechanistic aspects and application prospects of this method.

2 | Results and Discussion

Sputtering a gold target in an air plasma results in a mixed Au/Au_2O_3 thin film on the substrate. XPS confirms the presence of a significant Au(III) oxide fraction in these films shortly after deposition (Figure 1a). The Au 4f spectrum 6 h post-deposition exhibits two sets of peaks: the Au_2O_3 4f$_{7/2,5/2}$ doublet at binding energies ~89.9/86.2 eV, and the metallic Au 4f$_{7/2,5/2}$ at 87.7/84.0 eV. The oxidized gold accounts for roughly 60% of the total Au signal initially. To quantify the spontaneous reduction of Au(III), we recorded spectra for nominally identical films after ageing them in laboratory air for up to three weeks (Figure 1b–d). As shown in Figure 1b,c, the Au_2O_3 contribution gradually diminishes while the metallic Au peak area and sharpness increase. The overlaid spectra in Figure 1c show that this transformation occurs without the appearance of any new intermediate peaks, and the metallic peak narrows (full-width at half-maximum decreases from 1.08 to 0.81 eV) as the film's chemical environment homogenizes. Figure 1d summarizes the temporal evolution of the Au(III) fraction extracted from peak fitting. The decay follows a single-exponential dependence with a half-life of ~29 h and approaches a constant value of ca. 20% Au(III) at long times. These observations are consistent with the known metastability of Au_2O_3: room-temperature decomposition of gold(III) oxide is thermodynamically favored, with Au_2O_3 reverting to Au(0) and O_2 gas [12]. Early work by Tsai et al. showed that Au_2O_3 films formed by O_2-plasma treatment on Au spontaneously dissociate at 22°C, with first-order kinetics and a half-life of ~22 h [13]. Trace environmental reductants (e.g., hydrocarbons, CO, or humidity) can donate electrons to Au(III) in the film and are oxidized to produce harmless by-products while reducing Au_2O_3 to metallic gold [14]. Indeed, excluding oxygen and moisture is known to

dramatically slow down this reduction process [15]. In practical terms, our sputtered Au films initially contain a high oxide fraction but "self-heal" to a nearly metallic state within a few weeks at room temperature. The residual ~20% Au(III) signal observed after several weeks (Figure 1b–d) is consistent with the presence of more strongly bound oxygen species, such as subsurface oxygen or hydroxyl-like components, which have been identified in studies of gold oxides and shown to be much more stable than the stoichiometric Au_2O_3 that dissociates with a half-life of only a few tens of hours [12, 13, 15]. Observed aging must be accounted for in applications – devices should ideally utilize the fresh films or store them under inert conditions to preserve the oxidant (Au_2O_3) content.

The optical spectra of the fresh Au/Au_2O_3 films further reflect their composition. Figure 2a shows UV–vis transmission spectra for films ranging from 2.5 to 50 nm in thickness. Each spectrum is dominated by a broad absorption band at ~430 nm for the thinnest films, which redshifts slightly toward ~450 nm for thicker films, accompanied by increased overall absorbance with thickness. This ~430–450 nm band is attributable to interband electronic transitions in Au (the Au 5d to 6sp transition), which manifest in both metallic gold and its oxide forms [16]. Crucially, we do not observe a plasmon resonance around 520 nm that would be characteristic of discrete Au(0) nanoparticles [17]. The absence of a plasmon band, together with the XPS evidence of ~60% Au(III), indicates that the films behave optically as a uniform Au(oxide) continuum rather than as collections of metallic nanoparticles [18]. Figure 2b plots the absorbance at 430 nm vs film thickness: a remarkably linear trend is obtained from 2.5 up to 50 nm, consistent with Beer–Lambert absorption by a homogeneous medium. This linearity implies that the effective molar absorptivity of the Au/Au_2O_3 mixed phase is essentially constant over this thickness range [19]. Taken together, Figures 1 and 2 establish that our sputtered films initially contain a substantial reservoir of Au(III) (as Au_2O_3), which confers strong oxidizing power, while the minority metallic Au component forms a percolating but high-resistance structure (the films thinner than ~20 nm are not electrically conductive, as shown later).

We next explore how this built-in oxidant drives the polymerization of aniline. When a freshly sputtered Au/Au_2O_3-coated substrate is immersed in an acidic aniline solution, a visible green film of polyaniline appears within seconds. We monitored this reaction in real time by UV–vis spectroscopy and video (see Video S1). Figure 3 shows the time-resolved absorbance at 750 nm (a characteristic polaron band of doped PANI) during the polymerization on films of 5, 10, 15, and 20 nm Au/Au_2O_3. All traces exhibit a sigmoidal growth profile, with an induction period followed by a rapid rise and then saturation around 60 s. Thicker Au_2O_3 layers induce faster polymer growth: the initial slope of Abs_750 (from ~20 to 45 s) increases in the order 5 nm <10 nm < 15 nm < 20 nm, indicating a higher reaction rate with more oxidant available. Linear fits to these segments yield pseudo-first-order rate constants proportional to the Au_2O_3 thickness, confirming that the aniline polymerization rate is limited by the supply of electrons from Au(III) rather than by monomer diffusion. The photographic insets in Figure 3 (0, 20, 30, 40, 60 s) illustrate how each quadrant (with a given Au thickness) darkens as the emeraldine salt forms, and that the
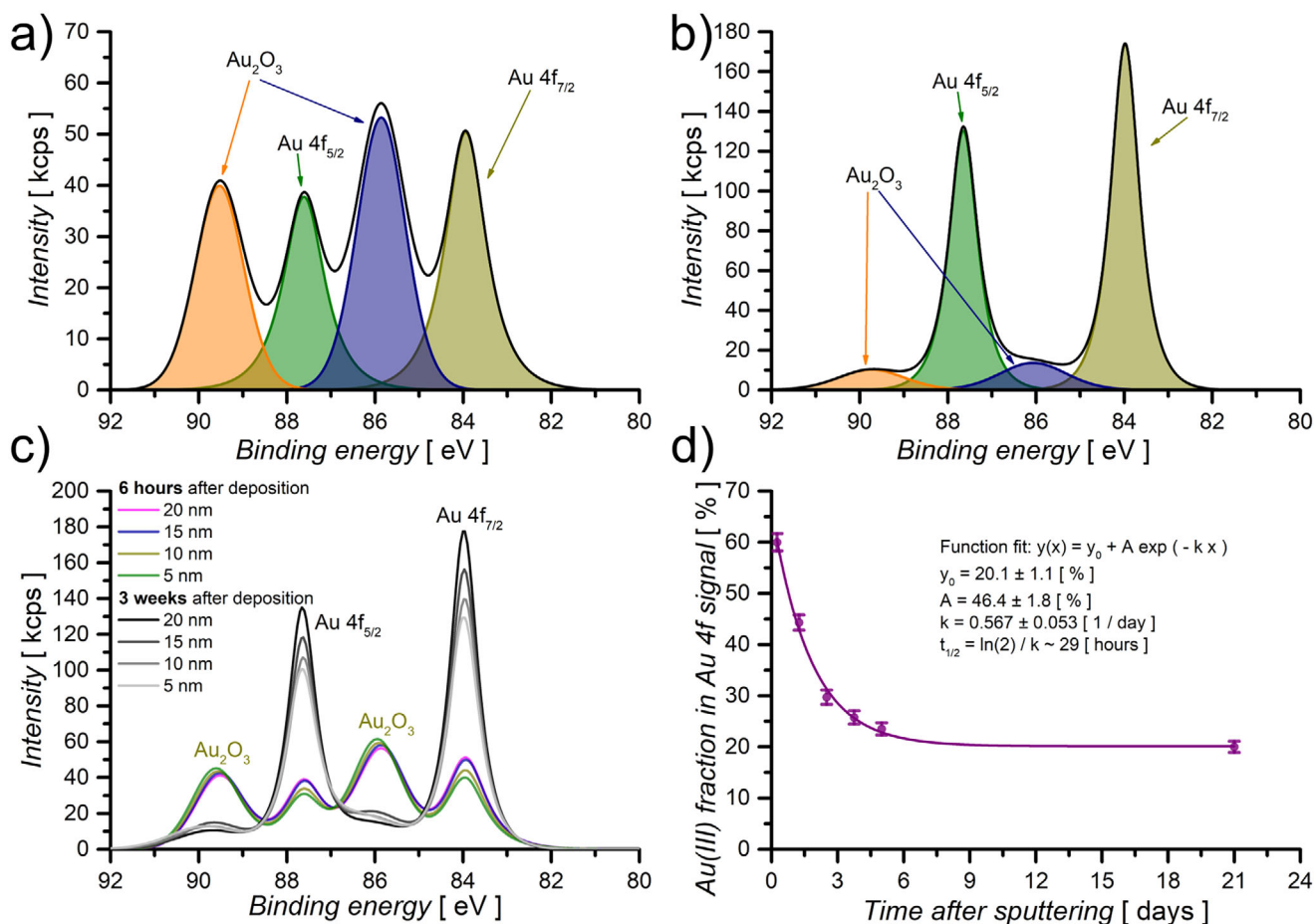
FIGURE 1 | High-resolution Au 4f XPS spectra of air-sputtered Au/Au$_2$O$_3$ nanofilms, and their temporal evolution. (a) Spectrum recorded 6 h after deposition, consisting of an Au$_2$O$_3$ doublet (peaks at 89.9 and 86.2 eV) alongside a metallic Au(0) doublet (87.7 and 84.0 eV). (b) Spectrum of the same film after ageing for 3 weeks in laboratory air, showing a substantial decrease of the Au$_2$O$_3$ signal. (c) Comparison of Au 4f spectra for films with different nominal Au thicknesses (5, 10, 15, and 20 nm) measured 6 h (colored lines) and 3 weeks (gray lines) after sputtering; in each case the oxide contribution shrinks while the metallic peaks sharpen. (d) Fraction of Au(III) in the Au 4f signal as a function of storage time in air, obtained from peak deconvolution of replicate films; the solid line is a single-exponential fit $y(x) = y_0 + A\,exp(-kx)$ giving an initial Au(III) content of ca. 66% and a residual long-time fraction of $20.1 \pm 1.1\%$ with a decay constant $k = 0.57 \pm 0.05\ day^{-1}$ (half-life $t_{1/2} \approx 29\ h$). Data points represent mean ± SD ($n = 4$ independent samples).
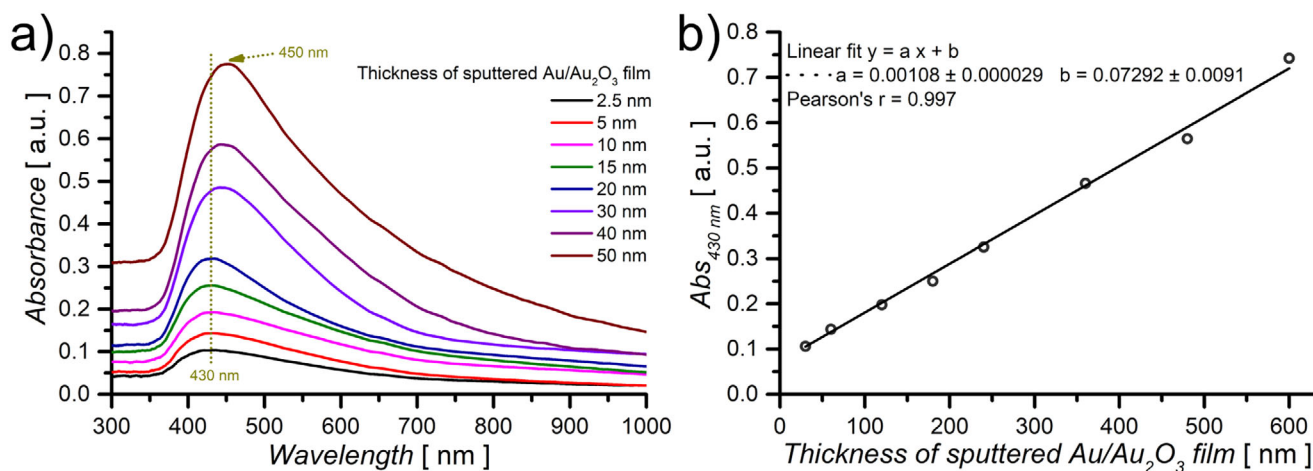
FIGURE 2 | Optical properties of sputtered Au/Au$_2$O$_3$ films on glass. (a) UV–vis transmission spectra for films of various nominal thickness (2.5, 5, 10, 15, 20, 30, 40, 50 nm). (b) Absorbance at 430 nm ($Abs_{430\,nm}$) plotted as a function of sputtered Au film thickness. A linear relationship is obtained from 2.5 up to ~50 nm thickness (Pearson's r = 0.997).
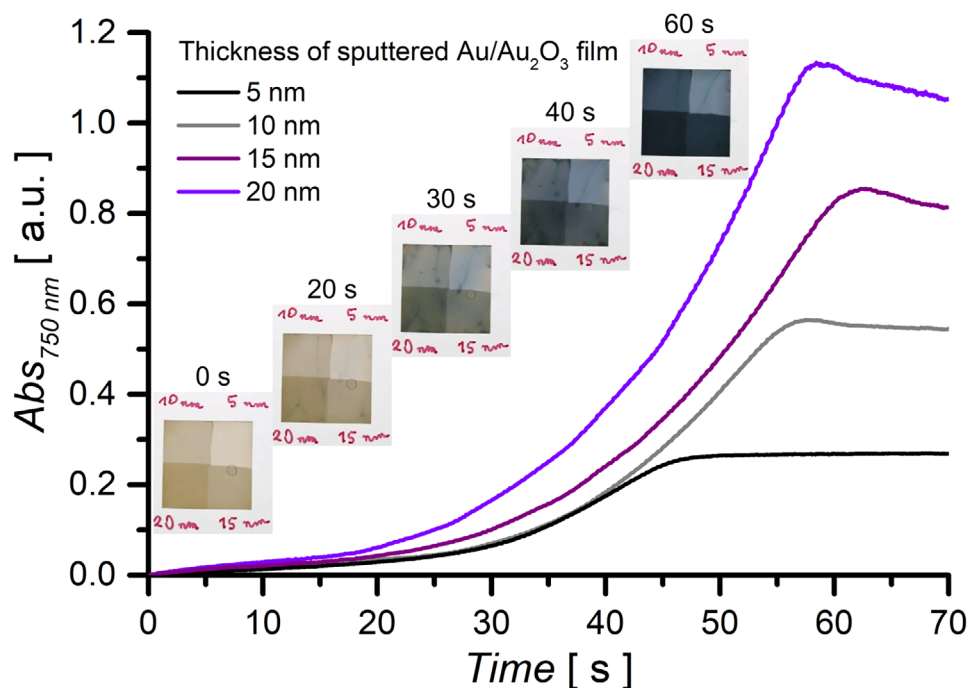
FIGURE 3 | Time-resolved absorbance at 750 nm (polaron band) during the oxidative polymerization of 0.30 M aniline in 1.0 M H_2SO_4 at 25°C on sputtered Au/Au_2O_3 films of 5, 10, 15, and 20 nm thickness. Each curve is an individual experiment (background-corrected) showing a sigmoidal increase in $Abs_{750\ nm}$ as the emeraldine-salt PANI forms. Photographs (insets) of the four quadrants at selected times (0, 20, 30, 40, 60 s) correspond to movie frames from a recorded video.

20 nm quadrant reaches full intensity the fastest. Importantly, control experiments showed no polymerization under identical conditions on substrates lacking Au_2O_3: pristine glass, pure sputtered Au(0) (no oxide), and even Au/Au_2O_3 films aged to metallic Au—all remained unchanged in the aniline solution. The reaction proceeds equally fast in oxygen-free acid (30 min of N_2 purging) and in complete darkness, ruling out any contribution from dissolved O_2 or photochemical/plasmonic effects. Thus, the driving force for polymerization comes entirely from the solid-state oxidant (Au_2O_3) in our system.

Several features of this reagent-free polymerization are noteworthy. First, the autocatalytic kinetics (Figure 3) – the accelerating rate after induction – suggest that once a thin conductive layer of PANI forms, it facilitates electron transport from underlying Au_2O_3 to continue the reaction until the oxidant is exhausted. Indeed, a mechanistic picture emerges in which an initial monomolecular layer of emeraldine salt nucleates uniformly on the Au_2O_3 surface, providing a redox-active "platform" for further 3D growth as long as electrons can flow from the Au(III) sites through this emerging PANI layer. This scenario is analogous to earlier observations of surface-confined polymerizations on noble-metal oxides and self-assembled monolayers [20]. Second, the reaction self-terminates automatically and locally. Once the Au(III) in a given region has been reduced to Au(0), that region can no longer oxidize aniline, and polymerization stops. The final state is a composite of inert Au(0) nanoparticles embedded in a PANI matrix. This self-termination helps the polymer remain closely aligned with the original pattern. Our optical observations show no measurable broadening of the features within the micrometer-scale resolution of these techniques: the visible edge of the PANI film follows the underlying Au/Au_2O_3 pattern. The

polymer films replicate the shapes of the metal masks with high fidelity, eliminating the need for post-patterning or lift-off steps. Third, as implied above, no external oxidant or electrode is needed: the solid Au_2O_3 itself provides the oxidizing power and defines the spatial confines of the reaction. This represents a practical advantage over conventional chemical polymerizations, which offer limited spatial control unless combined with lithography [21], and is complementary to electropolymerization, which rely on pre-patterned electrodes and an applied bias [22]. In our case, the Au/Au_2O_3 layer itself must still be patterned (e.g., using a shadow mask or standard lithography), but once this is done the polymerization proceeds by simple immersion without further wet patterning of the polymer layer.

The overall stoichiometry of the reaction can be written simply as:

$$Au_2O_3 + 3\,(aniline-H^+) \rightarrow (PANI)_3 + 2\,Au + 3\,H_2O$$
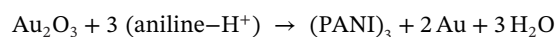
Each Au atom in Au_2O_3 thus provides three electrons, which is enough to oxidize 1.5 aniline dimers (three aniline monomers) to a polymer. The gold ions are reduced to Au(0) and left behind as part of the film. In the strongly acidic aqueous medium used here, the lattice oxygen of Au_2O_3 is protonated to water according to the reduction half-reaction $Au_2O_3 + 6\,H^+ + 6\,e^- \rightarrow 2\,Au + 3\,H_2O$. Thus, the oxygen atoms originally present in the oxide end up in H_2O rather than being released as molecular O_2. This is consistent with the absence of visible gas evolution and with the observation that the polymerization kinetics are unaffected when dissolved O_2 is removed by N_2 purging (Figure 3). Because the Au particles in the PANI film are electronically connected, the positive charge (holes) generated by the redox reaction can

rapidly percolate through the deposit. This means the oxidation wave propagates through the Au/Au_2O_3 layer until the local Au(III) reservoir is depleted, at which point the reaction in that locality ceases (abrupt end of growth is seen in Figure 3). We stress that oxygen in solution or any photonic effects are not needed – the driving force is entirely the internal redox energy of Au_2O_3.

To benchmark the redox properties of the sputtered films against conventional gold electrodes, we recorded cyclic voltammograms of a 3 mm polycrystalline Au disk either bare or sputter-coated with ~10 nm of Au/Au_2O_3 in 1.0 M H_2SO_4 (Figure S1). Both electrodes display the characteristic Au-oxide formation and reduction features, and the cathodic Au-oxide reduction peaks appear at 0.93 ± 0.02 V (polycrystalline Au) and 0.95 ± 0.02 V (Au/Au_2O_3) vs Ag/AgCl, respectively (Table S1). These values are fully consistent with reported Au-oxide reduction potentials in acidic media and lie well above the oxidation onsets typically used for electropolymerization of aniline ($\approx$0.8–0.9 V vs Ag/AgCl) [20] and pyrrole ($\approx$0.7–0.8 V vs Ag/AgCl) [23], as summarized in Table S2 [20, 23–27]. Therefore, the Au(0)/Au(III) provides a sufficient thermodynamic driving force for oxidizing aniline. Importantly, the oxidizing species in this couple is Au(III); metallic Au(0) shows no spontaneous polymerization. The fact that we observe reagent-free polymerization only on the nanocrystalline Au_2O_3 films indicates that the presence and morphology of Au(III)-oxide domains, rather than the redox potential of bare Au metal alone, govern the reactivity. On this basis, monomers with oxidation potentials below approximately 1.0 V vs Ag/AgCl, such as aniline derivatives and pyrrole, are expected to be compatible with the present reagent-free Au_2O_3-driven approach, whereas thiophene-type monomers, which oxidize at substantially higher potentials and are more hydrophobic, may require modified conditions.

Because the oxidant is patterned a priori, our method naturally supports spatially resolved polymer growth. In addition to rigid substrates like glass or silicon, we tested flexible substrates: for example, a cross-linked polydimethylsiloxane (PDMS) strip was sputter-coated with ~15 nm Au_2O_3 through a stencil mask and then dipped into aniline solution. The same rapid PANI formation occurred on PDMS (see Video S2), and the polymer adheres strongly even upon bending of the strip, with no cracking or delamination. This suggests the approach can be extended to stretchable or conformable electronics. We also note that sputtering in selected areas (using a shadow mask) yields PANI patterns directly – no photolithography or etching is required, unlike most previous methods for patterning conducting polymers.

After 60 s of reaction, the UV–vis spectra of the films show the characteristic emeraldine salt features of doped PANI. Figure 4a displays the optical absorption spectra of the PANI films obtained on different Au_2O_3 thicknesses after a fixed 2 min growth. All spectra have the expected emeraldine salt profile: a high-energy band (shoulder around 320–360 nm) from $\pi \rightarrow \pi^*$ transitions of benzenoid rings, and a broad polaron band spanning the visible to near-IR (with a center of approximately 750 nm) [28]. Notably, both the ~330 and ~430 nm sub-bands are more clearly visible in diffuse-reflectance measurements (discussed below) than in transmission mode [28], because the glass substrate absorbs below ~400 nm and scatters visible light. In Figure 4a, one can see that the polaron absorption (the long-wavelength tail) intensifies progressively as the underlying Au_2O_3 thickness increases from

2.5 to ~30 nm, indicating more PANI is produced with more oxidant available. Beyond ~30 nm of Au_2O_3, the increase in absorption tends to level off – e.g., the spectra for 40 and 50 nm in Figure 4a are quite close to that for 30 nm – suggesting that beyond a certain thickness, additional Au_2O_3 does not translate into proportionally more polymer (likely because the reaction becomes transport-limited or the film already becomes optically thick). This is quantified in Figure 4b, where the absorbance at 750 nm after 2 min is plotted vs. Au film thickness: a linear growth is seen from ~2.5 to ~30 nm (dashed fit line, $R^2 = 0.996$), but the points at 40 and 50 nm fall below this trend. Thus, under our conditions, an Au_2O_3 layer thicker than ~30 nm does not fully contribute to polymerization before the reaction stops. This is consistent with the self-terminating nature of the process – once a continuous PANI film has formed (providing an electronic pathway), further polymerization may slow or stop even if some Au(III) remains unreacted in deeper pockets, especially if the polymer blocks monomer transport or if the local redox potential has dropped below the threshold. In summary, the amount (thickness) of PANI produced is roughly proportional to the amount of Au_2O_3 up to a practical limit of ~30 nm in our system.

To gain more insight into the PANI's optical characteristics without substrate interference, we recorded diffuse-reflectance UV–vis spectra on the PANI/Au films. Figure 5a shows the reflectance spectrum of a representative PANI-ES film (from a 10 nm Au_2O_3 sample). In reflection, all three hallmark bands of emeraldine salt are clearly visible: an intense peak at ~350 nm (assigned to the $\pi \rightarrow \pi^*$ transition of the benzenoid units), a shoulder around 430 nm (polaron to π^* transition), and a broad absorption extending beyond 700 nm (delocalized polaron band in the near-IR) [28]. These features were present in transmission (Figure 4a) but were partly masked by glass absorption at the blue end. The diffuse-reflectance measurement confirms that our polymer is indeed in the emeraldine salt oxidation state (half-oxidized, protonated PANI) immediately after growth, with no need for additional doping [29]. Furthermore, resonance Raman spectroscopy (785 nm excitation) was used to verify the molecular structure of the polymer. The Raman spectrum (Figure 5b) of a PANI-ES film (on 10 nm Au) shows all the expected vibrational bands of protonated emeraldine: e.g., a C$-$N$^+$ stretching mode around 1270 cm^{-1}, a benzenoid C$=$C stretching at ~1500–1510 cm^{-1}, and a quinonoid C$=$C at ~1600 cm^{-1} [30]. The observed peak positions and their relative intensities are in excellent agreement with literature data for emeraldine salt. In particular, the prominent band at 1271 cm^{-1} (marked in Figure 5b) is characteristic of the delocalized polaronic form of PANI [30]. The fact that these vibrational signatures match those of well-characterized PANI-ES indicates that the polymer produced by our method is structurally the same as conventionally synthesized emeraldine salt polyaniline (no significant structural defects or alternate oxidation states). We note that no peaks for Au–ligand complexes are present; the polymer is not doped with gold species, since Au(0) is insoluble and remains as metallic nanoparticles in the film.

In addition, XPS survey spectra of PANI-ES films grown on Au/Au_2O_3 substrates with different underlying Au thicknesses (5 and 20 nm; Figure S2) show strong and nearly identical N 1s (~400 eV), C 1s (~285 eV), and S 2p (~168–170 eV) signals (Figure S2a). The similar N/S ratios for the two samples indicate that the
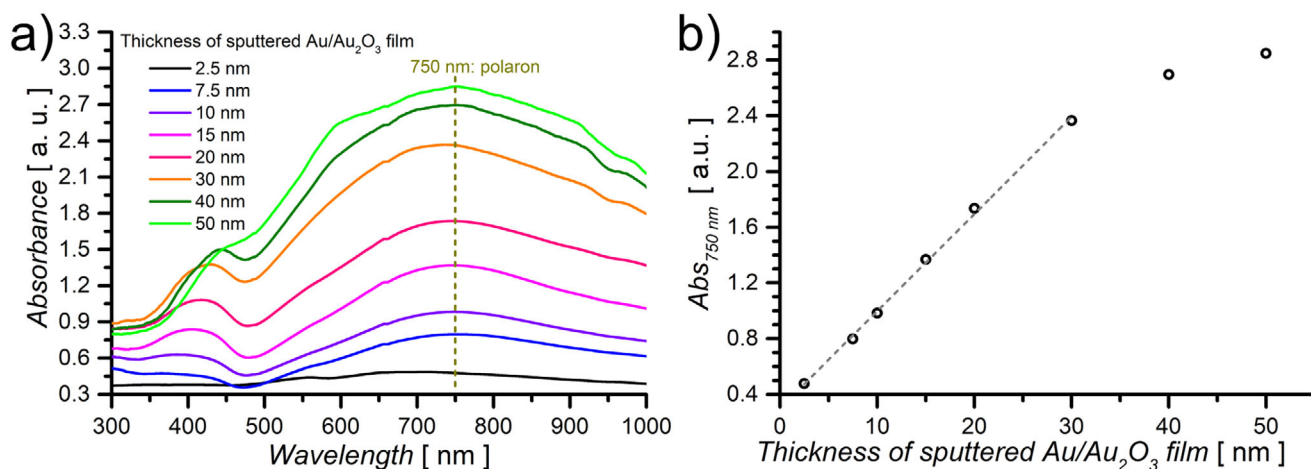
FIGURE 4 | Optical absorption of polyaniline films grown on Au/Au_2O_3. (a) UV–vis spectra of PANI (emeraldine salt form) obtained after 2 min of reaction on sputtered Au films of various thickness (2.5–50 nm). The spectra are background-corrected. (b) Peak absorbance at 750 nm as a function of Au/Au_2O_3 film thickness. A linear increase is observed up to ~30 nm (dashed line fit, $R^2 \approx 0.996$).

polymer composition and protonation level are independent of the Au/Au_2O_3 thickness. In the same spectra, the Au 4f envelope can be fitted solely with a metallic Au(0) doublet (Figure S2b), with no detectable Au(III) component, confirming that the initial Au_2O_3 is completely reduced during aniline polymerization.

Having established the chemical identity of the polymer, we next examined its electrochemical behavior. Cyclic voltammetry (CV) was performed to probe the redox transitions of the PANI film. Because the as-grown PANI on sputtered Au_2O_3 rests on a discontinuous (nonconductive) Au network, we adapted the sample for CV by using a bulk Au electrode as a substrate: a 3 mm diameter polished gold disk was sputtered with ~10 nm Au/Au_2O_3, reacted with aniline for 120 s, then rinsed and transferred to an electrolyte. In this configuration, the underlying metallic gold disk serves as a current collector, ensuring good electrical contact to the entire PANI film. Figure 6 shows a representative cyclic voltammogram of the PANI on Au (recorded

in 1.0 M H_2SO_4, sweep rate 100 mV s^{-1}). Two well-defined redox couples are observed, centered at approximately +0.15 V (A/A') and +0.81 V (B/B') vs Ag/AgCl. These correspond to the known redox transitions of polyaniline: the first pair (A/A') at ~0.0–0.3 V is the leucoemeraldine (fully reduced) to emeraldine salt (half-oxidized) conversion, and the second pair (B/B') at ~0.75–0.87 V is the emeraldine to pernigraniline (fully oxidized) conversion [31]. The small peak-to-peak separations (<120 mV) indicate fast, reversible proton-coupled electron transfer in both transitions, typical of a well-adhered PANI film. A minor feature around 0.5 V (marked C/C′) is also visible; this could be due to a low-level quinonoid impurity or some structural defect-related redox process [32], but it constitutes only a tiny fraction of the total charge and is represented schematically by the p-benzoquinone/hydroquinone couple drawn in the central inset of Figure 6. Notably, the voltammetric peaks remain almost unchanged over repeated scans (less than 2% change in peak currents after 5 cycles), demonstrating that the PANI film is
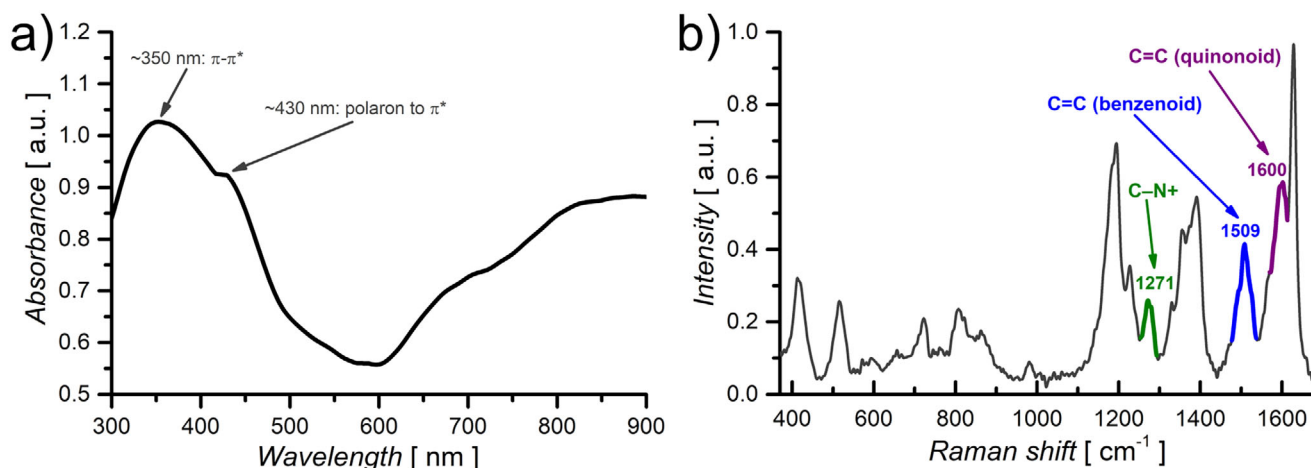

FIGURE 5 | Spectroscopic characterization of PANI confirming the emeraldine salt form. (a) Diffuse-reflectance UV–vis spectrum of a PANI film grown on a 10 nm Au/Au_2O_3 layer (on glass). (b) Resonance Raman spectrum of an emeraldine-salt PANI film on 10 nm Au/Au_2O_3 (785 nm excitation). The characteristic bands of PANI-ES are highlighted and assigned: ~1271 cm^{-1} (C—N$^+$ stretching of polaronic segments), ~1509 cm^{-1} (benzenoid C=C stretching), and ~1600 cm^{-1} (quinonoid C=C stretching). For clarity, only these diagnostic peaks are labeled.
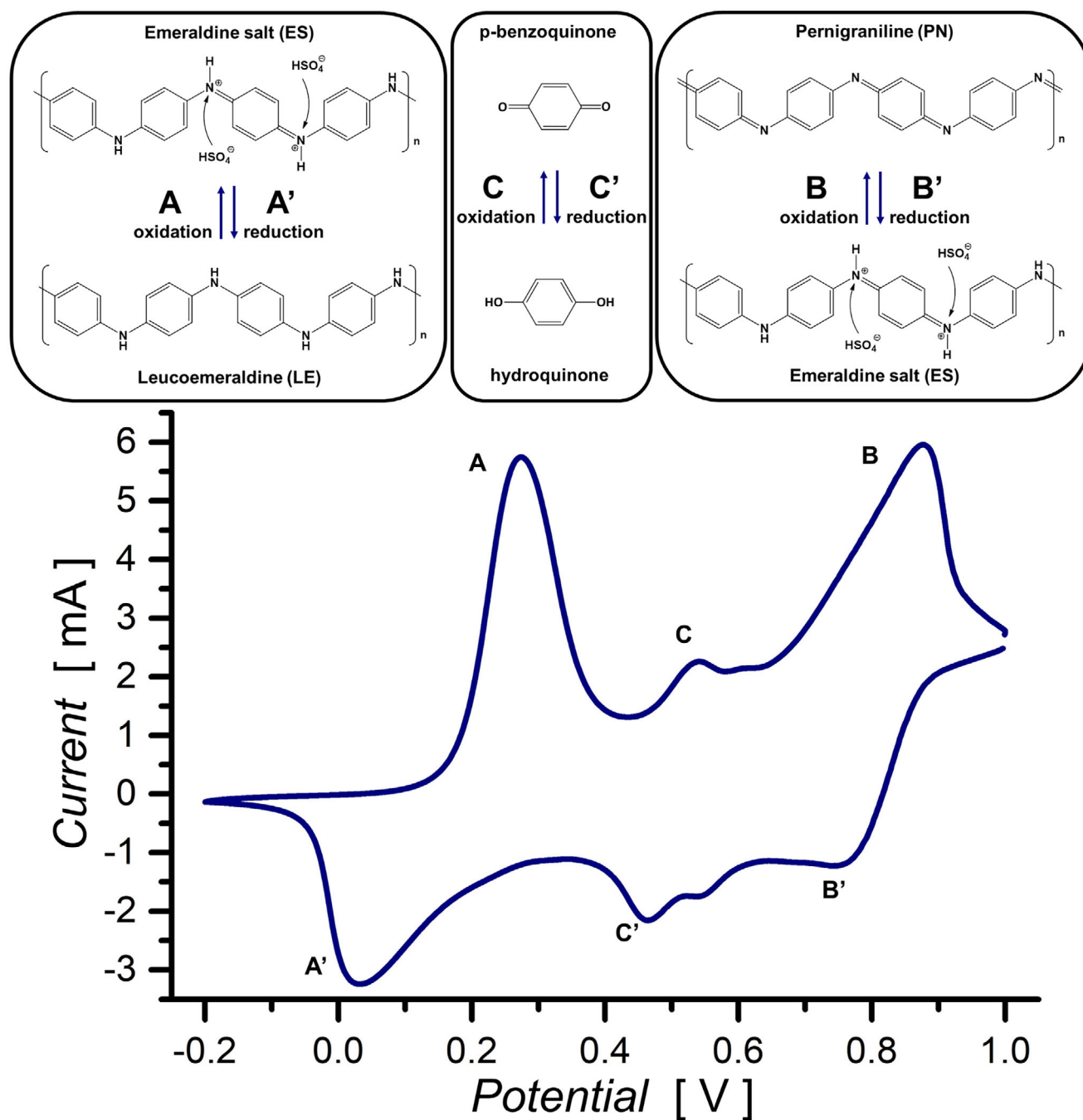
FIGURE 6 | Cyclic voltammogram of an aniline-grown PANI film, demonstrating its redox behavior. The PANI was synthesized on a 10 nm Au/Au$_2$O$_3$ coating sputtered onto a gold disk electrode (3 mm diameter), then cycled in 1.0 M H$_2$SO$_4$ (reference: Ag/AgCl; scan rate: 100 mV s^{-1}). The inset diagrams depict the chemical structures and protonation states of the polymer in each redox state and schematically illustrate the three redox couples observed in the CV: A/A'—leucoemeraldine ↔ emeraldine salt; C/C'—a minor p-benzoquinone/hydroquinone-type defect couple; and B/B'—emeraldine salt ↔ pernigraniline.

mechanically robust and electrochemically stable on the Au substrate. The insets in Figure 6 illustrate the molecular structures involved in the two main redox transitions: A/A' corresponds to the protonation/deprotonation and oxidation of leucoemeraldine (fully reduced, colorless) to emeraldine salt (half-oxidized, conducting, green), while B/B' is the oxidation/reduction between emeraldine salt and pernigraniline (fully oxidized, blue). The strong redox activity observed confirms that our PANI-ES is electroactive and suggests good electronic connectivity across the polymer/Au interface. We emphasize that in practical devices, if a conductive underlayer is desired for electrical readout, one can simply sputter a thicker Au film (≥20 nm) so that it becomes continuous; however, in many applications (e.g., sensors, coatings) the polymer itself serves as the conductor and the initial metal can remain discontinuous as in our method.

Beyond spectroscopic and electrochemical evidence, the morphology and elemental distribution of the PANI films provide
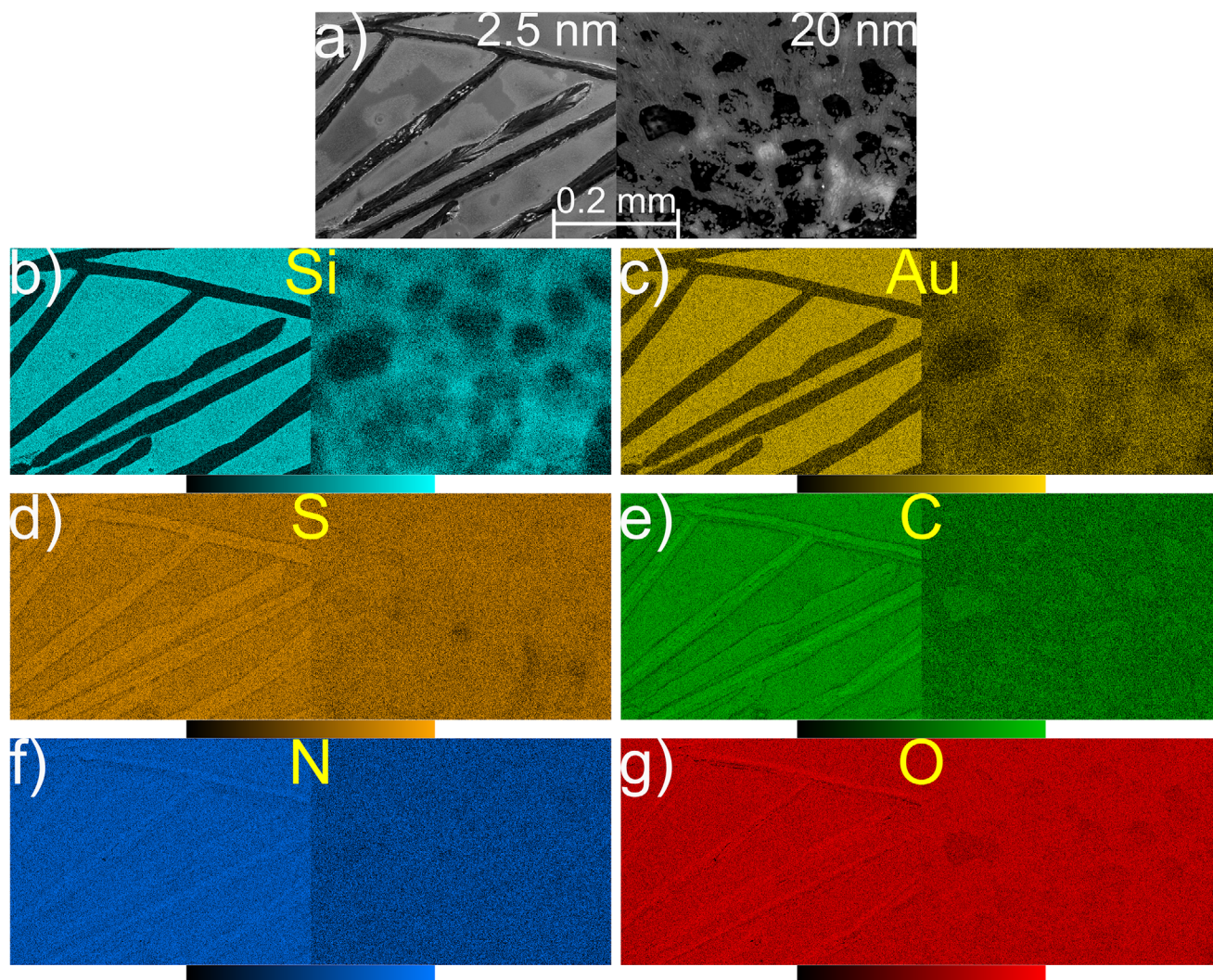
FIGURE 7 | SEM and EDS elemental mapping of polyaniline films grown on Au/Au$_2$O$_3$ layers of different thickness. (a) Secondary-electron images of PANI formed on 2.5 nm (left) and 20 nm (right) Au/Au$_2$O$_3$ films (scale bar: 0.2 mm). (b–g) Corresponding EDS maps of Si, Au, S, C, N, and O, respectively, recorded over the same areas and with the same parameters (left halves: 2.5 nm Au/Au$_2$O$_3$; right halves: 20 nm Au/Au$_2$O$_3$).

additional insight into the growth mechanism. We therefore performed SEM imaging combined with EDS mapping for PANI-ES films grown on two Au/Au$_2$O$_3$ thicknesses, 2.5 and 20 nm (Figure 7). For both samples, the Au/Au$_2$O$_3$ layer was sputtered uniformly over the glass substrate. In the SEM images, the PANI-ES coating appears continuous but exhibits elongated darker regions on a lighter background. These darker domains correspond to locally thicker PANI that most likely forms during the final stage of polymerization and drying after withdrawal from the aniline solution. The EDS maps for the 2.5 nm sample (left halves of panels Figure 7a–g) show that the Si and Au signals are strongly attenuated in the dark domains and highest in the lighter background, whereas the C, N, S, and O signals are present across the entire surface. This indicates that both regions contain the same PANI-ES composite, but the thicker PANI in the dark stripes efficiently screens the underlying glass and gold. For the 20 nm sample (right halves of panels Figure 7a–g), the PANI-ES layer is overall much thicker; consequently, the Si and Au signals are only weakly visible and largely confined to small defects, while the maps of C, N, S, and O become almost homogeneous. The mapping, therefore confirms that the apparent light and dark

areas in the SEM images arise from local variations in PANI thickness rather than from compositional differences.

To quantify how the film thickness evolves with the amount of Au$_2$O$_3$, we complemented the mapping with SEM and point EDS measurements on films grown on 2.5, 5.0, 7.5, and 20 nm Au/Au$_2$O$_3$ (Figure S3). For the thinnest case (2.5 nm), the brighter "light" regions still contain detectable nitrogen and sulfur (N ≈ 4 at.% and S ≈ 3 at.%), together with a significant Si fraction from the glass substrate (≈ 14 at.%), consistent with an ultrathin, nearly monomolecular PANI-ES layer. The darker regions are enriched approximately two-fold in N and S and show a reduced Si contribution, confirming that they correspond to thicker PANI-ES domains. With increasing Au/Au$_2$O$_3$ thickness, the N and S contents increase, and the Si signal systematically decreases, indicating a gradual transition from monolayer-plus-island coverage to a laterally continuous multilayer film. At 7.5 and 20 nm Au/Au$_2$O$_3$ the Si content drops to ≈3–2 at.% while N and S reach ≈9–10 at.% and 6–8 at.%, respectively, consistent with a robust PANI-ES coating that largely screens the substrate.
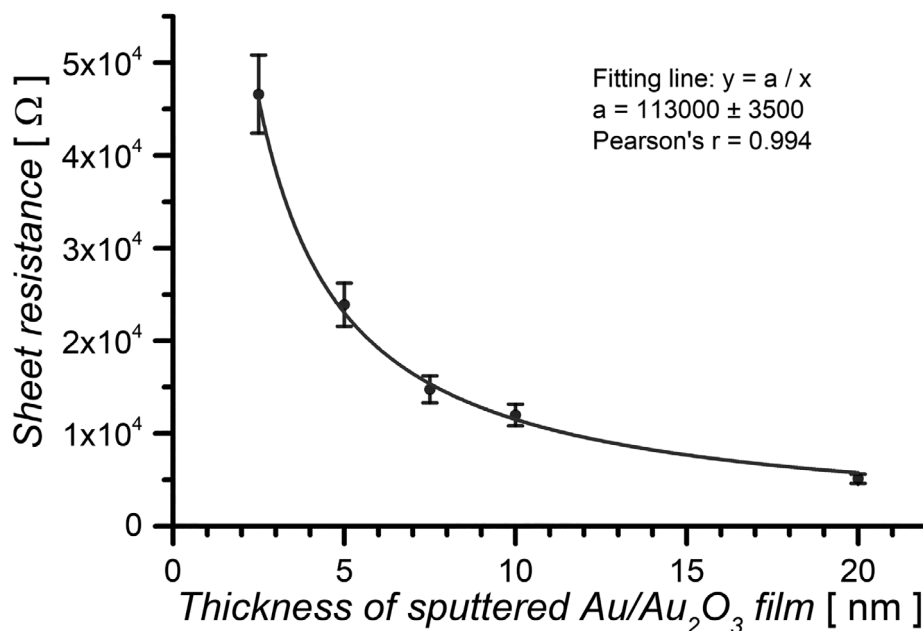
FIGURE 8 | Sheet resistance of PANI films as a function of initial Au/Au$_2$O$_3$ thickness. A hyperbolic fit describes the data, consistent with an approximately inverse proportionality. Each data point represents the mean sheet resistance obtained from $n = 5$ measurements at different positions on a substrate; error bars indicate $\pm$ SD.

Taken together, the SEM/EDS data support a Stranski–Krastanow-type growth mechanism: an ultrathin, laterally continuous emeraldine-salt wetting layer forms first on the Au$_2$O$_3$ surface, followed by the nucleation and growth of thicker 3D PANI domains once the surface is saturated [33, 34]. Such granular morphologies and thickness variations are characteristic of chemically and electrochemically synthesized PANI films and remain compatible with good electronic and electrochemical performance in devices such as electrochromic windows, supercapacitors, and chemiresistive sensors [2, 3, 33, 34].

Another consequence of the discontinuous nature of our sputtered Au films is their electrical behavior during polymerization. As noted, Au/Au$_2$O$_3$ layers thinner than ~20 nm are not percolating, so initially they are essentially non-conductive (sheet resistance >10 MΩ for ≤20 nm Au). This means they serve purely as a chemical initiator and template for PANI, rather than as an electrode. Only after the PANI network grows and spans the gaps does macroscopic conductivity emerge in the composite film. Figure 8 plots the sheet resistance (R_s) of the PANI-coated films as a function of the underlying Au thickness. As the Au/Au$_2$O$_3$ (and thus PANI) thickness increases, the sheet resistance drops dramatically – roughly following an inverse relationship $R_s \propto 1/(\text{thickness})$. For the thickest polymer films (on 20 nm Au), R_s is on the order of 10^3 Ω, whereas for the thinnest monolayer-like film (on 2.5 nm Au) R_s exceeds 10^5 Ω. The solid curve in Figure 8 is a hyperbolic fit ($R_s = a/x$) which matches the data well (Pearson r = 0.994), supporting that each incremental nm of Au$_2$O$_3$ yields a proportional increase in PANI thickness/conductivity (at least up to the percolation threshold of the Au). Beyond simply confirming that thicker polymer films are more conductive, this trend reinforces the idea that the amount of polymer is dictated by the amount of Au$_2$O$_3$ oxidant available. Once the PANI forms a continuous film, the composite becomes electrically conducting despite the starting Au/Au$_2$O$_3$ being non-continuous.

3 | Conclusion

In conclusion, our findings establish magnetron-sputtered Au/Au$_2$O$_3$ nanofilms as intrinsic, solid-state oxidants that can trigger the ultrafast (≤ 60 s) formation of polyaniline directly on a variety of substrates under ambient conditions, without any added chemical reagents. This approach yields electronically conductive PANI (emeraldine salt) films in a single step at room temperature. Because the Au$_2$O$_3$ is patterned during deposition and is consumed during polymerization, the method provides spatially confined polymer growth defined by the pre-patterned oxidant and avoids post-growth wet lithography of the conducting polymer. The oxidant is still consumed stoichiometrically, but it is immobilized in the device and converted into metallic Au rather than released as soluble sulfate or nitrate waste in the electrolyte. The native Au(III) reservoir in the film controls both the reaction kinetics (faster growth with thicker oxide) and the automatic self-termination of the polymerization, thereby preserving the fidelity of patterns – the polyaniline forms only where intended and stops by itself once the local oxidant is exhausted. We demonstrated that this technique can produce high-quality PANI films on rigid and flexible substrates alike, suggesting immediate applications such as the in situ fabrication of hole-transport layers in organic electronic devices, conductive polymer electrodes for neural interfaces, disposable chemiresistive sensors, and corrosion-resistant conductive traces on temperature-sensitive plastics. More broadly, this work showcases the untapped potential of metastable noble-metal oxides as "self-contained" redox reagents that combine chemical specificity with top-down patterning capability. We anticipate that this concept – using a thin-film metal oxide as both a patterned template and an internal oxidant

– will inspire analogous self-terminating polymerizations or oligomerizations in other conducting polymer systems and redox-active materials, opening new avenues for reagent-free nanofabrication in organic electronics and bioelectronics.

4 | Experimental Section

4.1 | Materials

Aniline (ACS reagent, ≥99.5%) was distilled under reduced pressure and stored under nitrogen at 4°C prior to use. Sulfuric acid (H_2SO_4, 95–98%) was purchased from Avantor and used as received. Glass coverslips (22 × 22 mm, thickness #1) were obtained from Thermo Fisher Scientific. Polydimethylsiloxane (PDMS) strips were prepared by casting Sylgard 184 (Dow Corning) and curing at 60°C for 4 h. All water used was ultrapure (18.2 MΩ cm).

4.2 | Substrate Preparation

Glass coverslips were cleaned by soaking in 1 M HCl at 60°C for 24 h, then thoroughly rinsed with water. The slides were sonicated sequentially in pure water (3 × 30 min) and in 50%, 75%, and 95% ethanol/water mixtures (30 min each). They were stored in 95% ethanol and dried at 60°C for 30 min immediately before use. PDMS substrates were cleaned by brief sonication in 2-propanol and water, then air-dried.

4.3 | Gold Sputtering

Thin gold films were deposited by direct-current magnetron sputtering (MiniQ S sputter coater, Quorum Technologies, UK) using a 99.99% Au target. The chamber was evacuated and backfilled with ambient air to 5×10^{-2} mbar pressure. The plasma was ignited in this dilute air atmosphere (serving as both working gas and reactive gas). Pulsed sputtering was carried out for controlled times: 30 s (yielding ∼5 nm Au), 60 s (∼10 nm), 90 s (∼15 nm), 120 s (∼20 nm), with longer depositions achieved by repeating these intervals. A quartz crystal microbalance was used to calibrate the deposition rate (approximately 0.083 nm/s under these conditions). During sputtering, some native oxide formed as the hot Au atoms ejected from the target thermalized in the oxygen-containing plasma and condensed on the substrate. The result was a mixed Au/Au_2O_3 film. Films were deposited either uniformly or through physical masks (contact stencils or patterned shadow masks) to create patterned coatings. After sputtering, films were either used immediately or stored in a desiccator to minimize ambient ageing. Repeated depositions carried out on different days under identical sputtering conditions yielded Au/Au_2O_3 films with practically identical optical density at 430 nm (Figure 2b), indicating good run-to-run reproducibility of both thickness and composition over the substrate area.

4.4 | X-Ray Photoelectron Spectroscopy (XPS)

XPS was performed on a Kratos AXIS Supra instrument with a monochromatic Al Kα source (hν = 1486.7 eV). Spectra were calibrated against the Au $4f_{7/2}$ line at 84.0 eV binding energy (instrument calibrated per ISO 15472). Survey scans were collected at 80 eV pass energy and high-resolution scans (for Au 4f) at 20 eV pass energy, yielding a peak width of ∼0.8 eV for metallic Au $4f_{7/2}$. Charge neutralization was applied during measurement. Peaks were fitted using CasaXPS software, with a Shirley background and mixed Gaussian–Lorentzian line shapes: metallic Au(0) 4f peaks were fitted with an asymmetric GL(86) shape while Au(III) oxide peaks were fitted with a more Gaussian GL(30) profile. Atomic percentages were determined from peak areas using the instrument's sensitivity factors ($RSF_{Au4f} = 6.25$). For time-dependent studies, samples were measured ∼6 h after sputtering and then after ageing in ambient lab air at several later time points up to 3 weeks (stored uncovered).

4.5 | UV–Vis Spectroscopy

Optical absorption and diffuse-reflectance UV–vis measurements in transmission were made using an Ocean Optics DH-Mini halogen-deuterium light source and a Thorlabs CCS200 CMOS spectrometer (200–1000 nm range, 2 nm resolution). A custom holder was used to orient the sample horizontally with a 1 cm optical path of solution above it. The spectra were collected at normal incidence for absorption measurements, and the reflection spectrum was measured with the light beam incident at an angle of 45 degrees. To account for the glass substrate, a reference measurement with a blank glass slide was taken and used to correct the sample spectra. In situ kinetic experiments were performed by first recording a baseline spectrum of the Au-coated slide in 1.0 M H_2SO_4 (no aniline). Then 1.0 mL of aniline solution (0.30 M aniline in 1.0 M H_2SO_4, pre-adjusted to 25°C) was injected onto the horizontal slide, and spectra were acquired every 0.1 s for up to 90 s. The time evolution of absorbance at 750 nm was extracted from the spectral data without smoothing. Kinetic traces were reproducible for independent repeats on freshly sputtered films. All optical experiments were conducted at ∼25°C.

4.6 | Polyaniline Polymerization

Polymerization was carried out by simply immersing the Au/Au_2O_3-coated substrate into the aniline/H_2SO_4 solution. For consistency, we used 0.30 M aniline in 1.0 M H_2SO_4 (an acid concentration high enough to protonate aniline and the emerging polymer). This solution was freshly prepared and used within 5 min. Typically, 1 mL of solution was applied per ∼4 cm^2 substrate area (to ensure complete wetting). The reaction was allowed to proceed for a specified time (e.g., 60 s) and then quenched by rinsing the sample with 1.0 M H_2SO_4 (which keeps the polymer in its doped state but removes unreacted monomer and soluble oligomers). The sample was then dried in air. In the present study, we routinely coated substrates with areas between 1 and 4 cm^2 (glass coverslips up to 22 × 22 mm and PDMS strips), and a single 60 s step produced a continuous PANI-ES film over the entire Au/Au_2O_3-covered area. Because the polymerization was limited by the amount of Au(III) in the sputtered film rather than by monomer depletion, the areal yield of the product was most naturally expressed in terms of film thickness per unit area,

which can be increased by choosing a thicker Au_2O_3 underlayer (Figure 4b) or by sputtering larger substrate areas.

4.7 | Raman Spectroscopy

Raman spectra of PANI were collected on a Thermo Fisher DXR Raman microscope with a 785 nm diode laser (max 150 mW output, attenuated to ~1 mW at the sample). A $50 \times$ /0.5 NA objective was used to focus on the polymer film. Spectra were accumulated with 10 s exposure × 6 scans to improve signal/noise. Spectral calibration was verified using the 520,5 cm^{-1} band of a silicon wafer. Prominent Raman peaks were assigned based on literature for emeraldine salt and are given in Figure 5b.

4.8 | Electrical Measurements

Four-point probe measurements were performed to determine sheet resistance (R_s). A Jandel CYL-RM3000+ station with a collinear four-point head (tip spacing 1.0 mm, tip radius ~25 μm) was used. A constant current (1.00 mA) was sourced through the outer probes using a Keithley 2450 SMU, and the voltage drop between the inner probes was measured after a 2 s stabilization. For each sample, five different spots were measured (center and near each corner of the ~2 × 2 cm square) and averaged. The films measured included the Au/Au_2O_3 layer (as-sputtered) and the PANI-coated layer (after polymerization and rinsing, dried). For the thinnest films (<20 nm Au), the as-sputtered Au/Au_2O_3 was essentially insulating (voltage reading saturated for 1 mA current, indicating >10^7 Ω). After PANI growth, those films became somewhat conductive, and for thicker Au/PANI films the resistance dropped into the ~5 kΩ range (Figure 8). All measurements were done at room temperature (~25°C) in ambient atmosphere. The four-point probe mapping on each ~2 × 2 cm substrate showed only modest spatial variations of Rs within a given film, confirming that the PANI/Au composite is laterally uniform at the scale relevant for device applications.

4.9 | Cyclic Voltammetry

Cyclic voltammetry (CV) was performed in a three-electrode glass cell using a 3 mm diameter polycrystalline Au disk as the working electrode, a Ag/AgCl (3 M KCl) reference electrode, and a Pt wire counter electrode. The Au disk was mechanically polished with 0.05 μm alumina slurry, rinsed thoroughly with deionized water, and sonicated in ethanol and water prior to use. For measurements of sputtered films, the cleaned Au disk was coated with ~10 nm Au/Au_2O_3 by direct-current magnetron sputtering under the conditions described above ("Gold Sputtering"). Unless stated otherwise, the electrolyte was 1.0 M H_2SO_4 at ~25°C, and the potential was scanned between 0.60 and 1.55 V vs. Ag/AgCl at a scan rate of 100 mV s^{-1}. Cyclic voltammograms of PANI-coated electrodes (Figure 6) were recorded under the same conditions after growing the PANI film by reagent-free polymerization on the sputtered Au/Au_2O_3 layer as described in the section "Polyaniline Polymerization".

4.10 | Scanning Electron Microscopy (SEM) and EDS

SEM imaging was carried out on a FEI Quanta FEG 250 field-emission SEM at 5–10 kV accelerating voltage. No conductive coating was applied to the samples (the PANI/Au films were sufficiently conductive to avoid charging at these voltages). Secondary electron images were collected at various magnifications to observe the surface morphology of the PANI films on different Au thicknesses. Energy-dispersive X-ray spectroscopy (EDX/EDS) was performed with an attached EDAX detector at 7 kV, acquiring spectra from selected regions (~100 μm^2 area) on each sample. Elemental composition (atomic %) was obtained by analyzing the characteristic X-ray peaks for C, N, O, Si, S, and Au, using an assumed standardless ZAF quantification. The results (averaged over 3 spots for each region) were summarized in Figure 7. The error of EDS for light elements was on the order of 0.5–1 at.% absolute. The samples examined were: PANI on Au (2.5, 5.0, 7.5, 20 nm) on glass, prepared as described above. Distinct "polymer-rich" (dark contrast) and "polymer-poor" (light contrast) areas were analyzed separately when present (for thinner Au cases). These correspond respectively to regions with thicker PANI vs regions with only the initial PANI monolayer. The SEM images in Figure 7 include insets highlighting how the higher magnifications correlate with the overview images.

4.11 | Video Microscopy

Real-time videos of the polymerization were recorded using a digital camera focused on the substrate. One example (Video S1) showed a 22 × 22 mm glass coverslip divided into four quadrants with 5, 10, 15, 20 nm Au_2O_3 (achieved by sputtering through a cross-shaped mask), upon which the aniline/H_2SO_4 solution was dropped. The differential timing of the green color appearance in each quadrant was clearly seen (with the 20 nm quadrant darkening first, etc.). Another video (Video S2) showed a flexible PDMS strip coated with 15 nm Au_2O_3, which was immersed in the monomer solution. The PDMS video demonstrated that the polymerization proceeded similarly on a bendable substrate and that the polymer film remained adherent under bending. Videos were captured at 30 fps and were played back at real-time speed. They qualitatively illustrate the same kinetics quantified in Figure 3.

4.12 | Statistical Analysis

Unless otherwise stated, experiments were repeated at least three times on independently prepared samples whenever this was experimentally feasible. Data points shown in the figures correspond to arithmetic means, and error bars, where present, represent one standard deviation (SD) of the mean. Error bars were plotted only when they were larger than the symbol size and could be reliably visualized. No formal statistical hypothesis testing or multiple-comparison procedures were applied in this study, and therefore no P values or significance symbols are reported. The statistical information relevant to each dataset (sample size n and definition of error bars) is summarized in the corresponding figure legends.

Conflicts of Interest

The authors declare no conflicts of interest.

Data Availability Statement

The data that support the findings of this study are available from the corresponding author upon reasonable request.

References

1. A. G. Macdiarmid, J. C. Chiang, A. F. Richter, and A. J. Epstein, "Polyaniline: A New Concept in Conducting Polymers," *Synthetic Metals* 18 (1987): 285–290, https://doi.org/10.1016/0379-6779(87)90893-9.

2. F. Gao, J. Mu, Z. Bi, S. Wang, and Z. Li, "Recent Advances of Polyaniline Composites in Anticorrosive Coatings: A Review," *Progress in Organic Coatings* 151 (2021): 106071, https://doi.org/10.1016/j.porgcoat.2020.106071.

3. B. P. Jelle and G. Hagen, "Performance of an Electrochromic Window Based on Polyaniline, Prussian Blue and Tungsten Oxide," *Solar Energy Materials and Solar Cells* 58 (1999): 277–286, https://doi.org/10.1016/S0927-0248(99)00009-4.

4. M. A. Bavio, G. G. Acosta, and T. Kessler, "Polyaniline and Polyaniline-Carbon Black Nanostructures as Electrochemical Capacitor Electrode Materials," *International Journal of Hydrogen Energy* 39 (2014): 8582–8589, https://doi.org/10.1016/j.ijhydene.2014.01.018.

5. C.-W. Lin, S. Xue, C. Ji, S.-C. Huang, V. Tung, and R. B. Kaner, "Conducting Polyaniline for Antifouling Ultrafiltration Membranes: Solutions and Challenges," *Nano Letters* 21 (2021): 3699–3707, https://doi.org/10.1021/acs.nanolett.1c00968.

6. H. Kim, Y. Won, H. W. Song, Y. Kwon, M. Jun, and J. H. Oh, "Organic Mixed Ionic–Electronic Conductors for Bioelectronic Sensors: Materials and Operation Mechanisms," *Advanced Science* 11 (2024): 2306191, https://doi.org/10.1002/advs.202306191.

7. Y. Cao, A. Andreatta, A. J. Heeger, and P. Smith, "Influence of Chemical Polymerization Conditions on the Properties of Polyaniline," *Polymer* 30 (1989): 2305–2311, https://doi.org/10.1016/0032-3861(89)90266-8.

8. N. V. Blinova, J. Stejskal, M. Trchová, I. Sapurina, and G. Ćirić-Marjanović, "The Oxidation of Aniline with Silver Nitrate to Polyaniline–Silver Composites," *Polymer* 50 (2009): 50–56, https://doi.org/10.1016/j.polymer.2008.10.040.

9. K. Mallick, M. J. Witcomb, A. Dinsmore, and M. S. Scurrell, "Polymerization of Aniline by Auric Acid: Formation of Gold Decorated Polyaniline Nanoballs," *Macromolecular Rapid Communications* 26 (2005): 232–235, https://doi.org/10.1002/marc.200400513.

10. Y. Y. Smolin, M. Soroush, and K. K. S. Lau, "Oxidative Chemical Vapor Deposition of Polyaniline Thin Films," *Beilstein Journal of Nanotechnology* 8 (2017): 1266–1276, https://doi.org/10.3762/bjnano.8.128.

11. D. Roy, A. Pal, and T. Pal, "Electrochemical Aspects of Coinage Metal Nanoparticles for Catalysis and Spectroscopy," *RSC Advances* 12 (2022): 12116–12135, https://doi.org/10.1039/D2RA00403H.

12. L. K. Ono and B. Roldan Cuenya, "Formation and Thermal Stability of Au$_2$O$_3$ on Gold Nanoparticles: Size and Support Effects," *The Journal of Physical Chemistry C* 112 (2008): 4676–4686, https://doi.org/10.1021/jp711277u.

13. H. Tsai, E. Hu, K. Perng, M. Chen, J.-C. Wu, and Y.-S. Chang, "Instability of Gold Oxide Au$_2$O$_3$," *Surface Science* 537 (2003): L447–L450, https://doi.org/10.1016/S0039-6028(03)00640-X.

14. T. Yokoyama, Y. Matsukado, A. Uchida, Y. Motomura, K. Watanabe, and E. Izawa, "Uptake of Au(III) Ions by Aluminum Hydroxide and Their Spontaneous Reduction to Elemental Gold (Au(0))," *Journal of Colloid and Interface Science* 233 (2001): 112–116, https://doi.org/10.1006/jcis.2000.7260.

15. M. Higo, Y. Matsubara, Y. Kobayashi, M. Mitsushio, T. Yoshidome, and S. Nakatake, "Formation and Decomposition of Gold Oxides Prepared by an Oxygen-Dc Glow Discharge from Gold Films and Studied by X-Ray Photoelectron Spectroscopy," *Thin Solid Films* 699 (2020): 137870, https://doi.org/10.1016/j.tsf.2020.137870.

16. T. Barman, A. A. Hussain, B. Sharma, and A. R. Pal, "Plasmonic Hot Hole Generation by Interband Transition in Gold-Polyaniline," *Scientific Reports* 5 (2015): 18276, https://doi.org/10.1038/srep18276.

17. X. Huang and M. A. El-Sayed, "Gold Nanoparticles: Optical Properties and Implementations in Cancer Diagnosis and Photothermal Therapy," *Journal of Advanced Research* 1 (2010): 13–28, https://doi.org/10.1016/j.jare.2010.02.002.

18. K. M. Cook and G. S. Ferguson, "Determination of the Wavelength-Dependent Refractive Index of a Gold-Oxide Thin Film," *The Journal of Physical Chemistry C* 115 (2011): 22976–22980, https://doi.org/10.1021/jp207031s.

19. A. Larena, G. Pinto, and F. Millán, "Using the Lambert-Beer Law for Thickness Evaluation of Photoconductor Coatings for Recording Holograms," *Applied Surface Science* 84 (1995): 407–411, https://doi.org/10.1016/0169-4332(95)00003-8.

20. Y. Lee, S. Chen, H. Tu, et al., "In Situ STM Revelation of the Adsorption and Polymerization of Aniline on Au(111) Electrode in Perchloric Acid and Benzenesulfonic Acid," *Langmuir* 26 (2010): 5576–5582, https://doi.org/10.1021/la903857x.

21. J. Stejskal and R. G. P. Gilbert, "Polyaniline. Preparation of a Conducting Polymer(IUPAC Technical Report)," *Pure and Applied Chemistry* 74 (2002): 857–867, https://doi.org/10.1351/pac200274050857.

22. J. Rivnay, R. M. Owens, and G. G. Malliaras, "The Rise of Organic Bioelectronics," *Chemistry of Materials* 26 (2014): 679–685, https://doi.org/10.1021/cm4022003.

23. B. C. Thompson, S. E. Moulton, J. Ding, et al., "Optimising the Incorporation and Release of a Neurotrophic Factor Using Conducting Polypyrrole," *Journal of Controlled Release* 116 (2006): 285–294, https://doi.org/10.1016/j.jconrel.2006.09.004.

24. T.-H. Le, Y. Kim, and H. Yoon, "Electrical and Electrochemical Properties of Conducting Polymers," *Polymers* 9 (2017): 150, https://doi.org/10.3390/polym9040150.

25. C. V. Manzano, O. Caballero-Calero, A. Serrano, P. M. Resende, and M. Martín-González, "The Thermoelectric Properties of Spongy PEDOT Films and 3D-Nanonetworks by Electropolymerization," *Nanomaterials* 12 (2022): 4430, https://doi.org/10.3390/nano12244430.

26. W. Fujita, N. Teramae, and H. Haraguchi, "Formation of Thiophene Oligomers and Polythiophene on a Roughened Gold Electrode Studied by Surface Enhanced Raman Scattering," *Chemistry Letters* 23 (1994): 511–514, https://doi.org/10.1246/cl.1994.511.

27. M. Saraji and A. Bagheri, "Electropolymerization of Indole and Study of Electrochemical Behavior of the Polymer in Aqueous Solutions," *Synthetic Metals* 98 (1998): 57–63, https://doi.org/10.1016/S0379-6779(98)00151-9.

28. P.-Y. Wong, S.-W. Phang, and A. Baharum, "Effects of Synthesised Polyaniline (PAni) Contents on the Anti-Static Properties of PAni-Based

Polylactic Acid (PLA) Films," *RSC Advances* 10 (2020): 39693–39699, https://doi.org/10.1039/D0RA07076A.

29. D. Dutta, T. K. Sarma, D. Chowdhury, and A. Chattopadhyay, "A Polyaniline-Containing Filter Paper That Acts as a Sensor, Acid, Base, and Endpoint Indicator and Also Filters Acids and Bases," *Journal of Colloid and Interface Science* 283 (2005): 153–159, https://doi.org/10.1016/j.jcis.2004.08.051.

30. M. C. Bernard and A. Hugot-Le Goff, "Quantitative Characterization of Polyaniline Films Using Raman Spectroscopy," *Electrochimica Acta* 52 (2006): 595–603, https://doi.org/10.1016/j.electacta.2006.05.039.

31. E. Song and J.-W. Choi, "Conducting Polyaniline Nanowire and Its Applications in Chemiresistive Sensing," *Nanomaterials* 3 (2013): 498–523, https://doi.org/10.3390/nano3030498.

32. M. Bláha, F. Marek, Z. Morávková, et al., "Role of p -Benzoquinone in the Synthesis of a Conducting Polymer, Polyaniline," *ACS Omega* 4 (2019): 7128–7139, https://doi.org/10.1021/acsomega.9b00542.

33. H. Okamoto, M. Okamoto, and T. Kotaka, "Structure Development in Polyaniline Films During Electrochemical Polymerization. II: Structure and Properties of Polyaniline Films Prepared via Electrochemical Polymerization," *Polymer* 39 (1998): 4359–4367.

34. D. S. Sutar, N. Padma, D. K. Aswal, S. K. Deshpande, S. K. Gupta, and J. V. Yakhmi, "Growth of Highly Oriented Crystalline Polyaniline Films by Self-Organization," *Journal of Colloid and Interface Science* 313 (2007): 353–358, https://doi.org/10.1016/j.jcis.2007.04.051.

Supporting Information

Additional supporting information can be found online in the Supporting Information section.

Supporting File 1: admt70654-sup-0001-SuppMat.pdf.

Supporting File 2: admt70654-sup-0002-VideoS1.mp4.

Supporting File 3: admt70654-sup-0003-VideoS2.mp4.